

# Effect of welding parameters on residual stresses in dissimilar joint of stainless steel to carbon steel

E. Ranjbarnodeh · S. Serajzadeh · A. H. Kokabi ·  
A. Fischer

Received: 15 October 2010 / Accepted: 17 December 2010 / Published online: 29 December 2010  
© Springer Science+Business Media, LLC 2010

**Abstract** In this study, a thermo-mechanical model was utilized to investigate the effects of welding parameters on the distribution of residual stresses in dissimilar TIG welds of low carbon and ferritic stainless steels. To solve the governing thermal and mechanical problems, a finite element program, ANSYS, was employed while the different aspects such as welding sequence and dilution were considered in the numerical solution. To validate the predictions, the model results were compared with the residual stresses measured by X-ray diffraction technique and a reasonable agreement was found. The results show that the magnitude of tensile residual stresses decrease as the welding current increases while lower residual stresses are produced in the longer samples. In addition, the magnitudes of residual stresses significantly decrease when a symmetric welding sequence is employed especially for the carbon steel part with the higher yield strength.

## Introduction

In arc welding operations residual stresses are introduced within the welded metal owing to the non-uniform temperature distribution and severe temperature gradients, while they may be responsible for brittle fracture, decreasing fatigue life as well as stress corrosion cracking

[1]. Dissimilar joints are made between two materials that are significantly different in chemical and/or mechanical properties. When dissimilar metals are joined by a fusion welding process such as TIG welding technique, mixing of the base metals and the filler metal results in the weld region to have different mechanical properties and this phenomenon affects the distribution of residual stress after welding operation. In this regard, appropriate designing of welding procedure of these joints is of importance to engineers and scientists. It should be noted that welding residual stresses and strains are influenced by many factors such as thermo-physical and mechanical properties of base metal, geometry of the weldment, heat input, and welding sequence. So far, there have been a few published studies on residual stresses in similar as well as dissimilar arc welding operations. For instance Choi and Mazumder [2] investigated the solidification and the residual stresses in the GMAW process for AISI 304 stainless steel. They found that welding residual stresses increase with the increase in welding speed. Paradowska et al. [3] studied the effect of heat input on residual stresses distribution. They reported that the heat input affects the value and distribution of residual stresses in the specimen while the transverse residual stresses were about half of the maximum value of longitudinal stresses. Teng and Lin [4] developed a model to evaluate the effects of welding speed, specimen size, mechanical constraint, and preheating on residual stresses. In another study, Teng et al. [5] evaluated the residual stresses with various types of welding sequences in single-pass welding. Katsareas and Yostous [6] developed two-dimensional and three-dimensional models to predict residual stresses distribution in a dissimilar joint between A508 and 1.4301 steels. Sahin et al. [7] used a two-dimensional finite element model to predict the residual stresses in a brazed joint between 1.0402 and brass (BS CZ107).

---

E. Ranjbarnodeh · S. Serajzadeh (✉) · A. H. Kokabi  
Department of Materials Science and Engineering,  
Sharif University of Technology, Tehran, Iran  
e-mail: serajzadeh@sharif.edu

A. Fischer  
Materials Science and Engineering, University Duisburg-Essen,  
Lotharstr. 1, 47057 Duisburg, Germany

Akbari et al. [8] developed a model to study the effects of the welding heat input on residual stresses in butt-welds of dissimilar pipe joints in which ferritic and austenitic stainless steels were used as the base metals.

Regarding the published works on dissimilar arc welding, further studies are required to evaluate thermo-mechanical responses of the weldment particularly under different welding conditions as well as welding sequences. In this study, a thermo-mechanical model is employed to evaluate the effects of welding parameters, welding sequence and dilution on the residual stresses in dissimilar butt joints of carbon and stainless steels produced by TIG welding process. To do so, a finite element software, ANSYS, is employed to perform the solution of the governing problems of heat transfer and elastic–plastic deformation. In order to verify the models results, the predictions are compared with the experimental data achieved from optical macro-graph of weld section and X-ray diffraction measurements.

### Mathematical model

Prediction of temperature cycles in welding operations is a main point in determining welding residual stresses and accordingly, the problem of heat conduction in the weldment should be solved firstly. The following equation can be used to describe temperature variations inside the parts are being welded:

$$\frac{\partial}{\partial x} \left( k \frac{\partial T}{\partial x} \right) + \frac{\partial}{\partial y} \left( k \frac{\partial T}{\partial y} \right) + \frac{\partial}{\partial z} \left( k \frac{\partial T}{\partial z} \right) = \rho C \frac{\partial T}{\partial t} \quad (1)$$

here  $T$  denotes the temperature,  $k$  the thermal conductivity,  $C$  the specific heat,  $\rho$  the density,  $t$  welding time, and  $z$ ,  $x$  and  $y$  show welding directions, transverse direction and thickness direction, respectively. At the beginning of the process, i.e.,  $t = 0$ , the entire model was at the room temperature while during welding, the following boundary conditions were taken into account. Convection–conduction boundary conditions were assumed on surface boundaries except for the region affected by the welding arc, as presented in Eq. 2:

$$-k \frac{\partial T}{\partial n} = h(T - T_a) \quad (2)$$

where “ $n$ ” denotes the normal direction to the surface boundary,  $T_a$  is the ambient temperature and “ $h$ ” is convection heat transfer coefficient. Convection coefficient was taken as 15 W/m<sup>2</sup>K for the surfaces in contact with ambient air. For the surfaces that are in contact with the backing plate, the convection coefficient was taken as 800 W/m<sup>2</sup>K.

Note that at the top surface of the sample where influenced by the moving arc, the boundary condition is given as Eq. 3:

$$k \frac{\partial T}{\partial y} = q(r) = \frac{\eta VI}{2\pi r'^2} \exp \left[ -\frac{1}{2} \left( \frac{r}{r'} \right)^2 \right] \quad (3)$$

where “ $n$ ” denotes the normal direction to the surface boundary,  $q(r)$  is the imposed surface heat flux from the arc,  $\eta$  is welding process efficiency,  $V$  is welding voltage,  $I$  is welding current, “ $r$ ” is the distance from the center of heat source and “ $r'$ ” is the Gaussian distribution parameter which is the radius of area to which 95% of energy is entered [1]. In this study, “ $r'$ ” was assumed to be 1.5 mm and  $\eta$  was taken as 0.6 [9].

It should be mentioned that the finite element software, ANSYS is employed to solve the above heat conduction problem. Regarding the thermal response of the material being welded, it is expected to produce severe temperature gradient close to the welding arc and therefore, very fine elements are required in weld pool region to achieve accurate results. Thus, the mesh is generated in such a way that the size of the elements increases exponentially in the transverse direction, i.e., the  $x$ -axis. The used mesh system is displayed in Fig. 1.

To include the effect of welding speed, a subroutine was developed to simulate the moving heat source in the model. A coordination system was defined and its origin located at the moving arc center. This program was also used to calculate the distances of the surface elements from the origin of the coordination system. At each time step, this origin was transferred to the position of “ $z \pm il_z$ ” where “ $i$ ” is the number of time step and “ $l_z$ ” is the element length in  $z$ -direction.

At the same time, the mechanical response of the weldment should be determined using equilibrium equation as mentioned in Eq. 4.

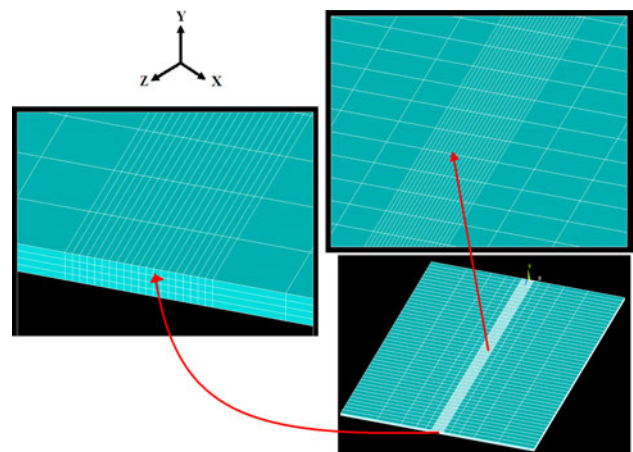


Fig. 1 The employed mesh system in the model

$$\sigma_{ij,j} + b_i = 0 \tag{4}$$

where  $\sigma_{ij}$  is the Cauchy stress tensor and  $b_i$  is the body force vector which are obtained from the thermal analysis. Note that the thermo-elastic–plastic constitutive equations based on the Von Mises yield criterion and the isotropic strain hardening rule, are utilized in the model [10]. In the mechanical part of the simulation, the essential boundary conditions were taken as  $u = 0$  for the origin of the coordination system and the normal displacement,  $u_y$ , was set to be zero at the bottom surface of the welded plates. Note that since the thermal elastic–plastic analysis is a non-linear path-dependent problem, the incremental calculations together with iterative solution techniques are used in the solution.

It is worth noting that in the short samples, 5,670 elements and 7,130 nodes are used while for the longer samples, 11,340 elements and 14,105 nodes have been used in the analysis. In addition, temperature-dependent material properties were employed for both stainless steel and low carbon steel parts. Tables 1, 2, and 3 show the thermo-physical properties of the employed steels at different temperatures. Note that the specific heat of stainless steel

**Table 1** Thermal conductivity of the carbon steel

Temperature (°C)	Thermal conductivity (W/m K)
20	51.5
800	29.7
1,500	29.7
2,000	30

**Table 2** Thermal conductivity of the stainless steel

Temperature (°C)	Thermal conductivity (W/m K)
20	25
500	30
1,400	30
2,000	90

**Table 3** Specific heat of the carbon steel

Temperature (°C)	C (J/kg K)
20	425
675	846
700	1,139
730	1,384
750	1,191
1,000	779
1,500	400

was assumed to be 460 J/kg K [11]. Furthermore, to consider the effect of fluid flow in the weld pool, the thermal conductivity was assumed to increase linearly above the melting point by a factor of about three [12, 13]. The thermal expansion coefficients of low carbon steel and stainless steel were taken as  $11.7 \times 10^{-6}$  and  $12 \times 10^{-6}$ , respectively.

In the solution procedure, the total duration of the joining process was divided into two main parts. The first part was allocated to complete welding stage and the remaining time was for performing the cooling stage. While during and after the welding process, the sample was fixed to prevent rigid body motion. Note that for the mechanical part of the simulation the results of thermal part were applied as the body force vector and as a result, the thermal stresses were calculated in each step based on the corresponding predicted temperature field at the same time step. In the other words, the thermo-mechanical problem was handled as a sequentially coupled one. Moreover, the effect of dilution was considered in the model. The dilution is defined as the weight of the base metal melted divided by the total weight of the weld metal. Dilution affects the chemical and mechanical properties of weld metal and consequently, the distribution of temperature in the weld zone is influenced by this phenomenon. Accordingly, the effect of dilution was taken into account by changing the weld zone material properties using MPCHG command in ANSYS. This command changes the material number of the specified elements between load steps in solution part of analysis. At each stage of solution, the temperature distribution of model was checked and the melted part of the joint was determined by selecting the elements with temperatures higher than the melting point, i.e., 1,500 °C for carbon steel and 1,400 °C for stainless steel. Then, the material properties of these elements were changed to the new material number using lever rule.

### Experimental procedure

Table 4 shows the chemical compositions of the steels used in welding experiments. The samples with dimensions of  $225 \times 80 \times 2$  (mm<sup>3</sup>) were welded by automatic TIG welding machine, while no filler was used. Table 5 shows the welding parameters used in the welding experiments including samples 105LP, 120LP, 135LP, and 120SP and

**Table 4** Chemical composition of welded base metals

Material	C	Si	Mn	Ni	Cr	Ti
Stainless steel (AISI409)	0.015	0.59	0.27	0.13	11.28	0.17
Carbon steel (CK4)	0.025	0.013	0.19	0.04	0.01	–

**Table 5** Welding parameters used in this study

Sample	Current (A)	Length (mm)	Speed (mm/s)	Voltage (v)	Welding sequence
105LP	105	450	3.56	13	Forward
120LP	120	450	3.56	13	Forward
135LP	135	450	3.56	13	Forward
120SP	120	225	3.56	13	Forward
120SS	120	225	3.56	13	Symmetric
120SB	120	225	3.56	13	Back-step

also it shows the welding conditions just used in the simulation including samples 105LP, 120SS, and 120SB. After welding operation, the distribution of the surface longitudinal stresses of sample 120SP along the  $x$ -axis at the position of  $z = 180$  mm was measured by means of X-ray diffraction technique. The residual stresses were measured in a region with the dimension of  $2 \times 4$  mm<sup>2</sup> at  $\psi$  angles 35°, 25°, 15°, and 10°, the Young modulus was assumed to be as 210 GPa and Poisson ratio of 0.3 while the target was Cr-K <sub>$\alpha$</sub>  and diffraction plane (211). In addition, after the welding process, a macro section from the middle of the joint line was prepared from two samples, i.e., 120LP and 135LP and the weld pool geometries were determined to verify the thermal part of the simulation.

## Results and discussion

Figure 2 compares the predicted weld pool geometry and the experimental observations for samples 120LP and 135LP. In addition, Table 6 shows the comparison between simulations and experimental results of the weld pool width under different welding conditions where in this table, “w1” and “w2” denote the width of the weld pool at the upper surface and the lower surfaces, respectively. Regarding Fig. 2 and Table 6, it can be seen that there is a reasonable agreement between the predictions and the experiments.

Figure 3 displays temperature distribution for the samples with different welding currents at the middle of the joint. As it is expected, the peak temperature and weld pool size increases in higher welding currents. For example, the maximum temperature increases from 2,276 to 2,635 °C as the welding current changes from 105 to 135 A. However, the weld pool shape as well as temperature distribution are asymmetric because of the different thermo-physical properties of the welded steels. Figure 4 also shows the temperature cycles at different pints of the sample 120LP. It is seen that the different thermo-physical properties of the base metals result in different temperature variations. Thermal diffusivity of the carbon steel is higher than the

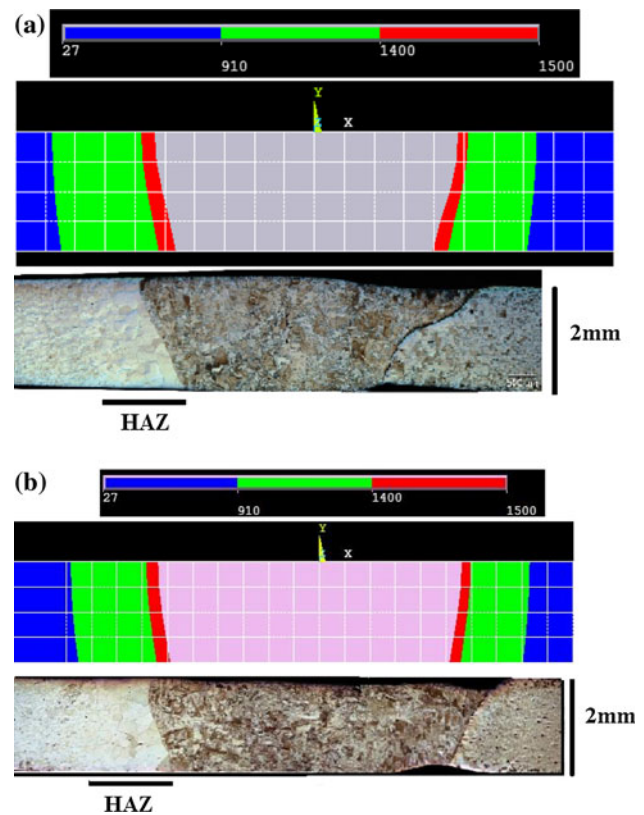


**Fig. 2** Comparison between the predicted and the observed weld pool, **a** sample 120LP, **b** sample 135LP

stainless steel which in turn, it causes higher temperatures at the stainless steel side of the weld.

The comparison between the experimental and the predicted distribution of longitudinal residual stresses for sample 120SP at the position of  $z = 180$  mm is presented in Fig. 5. Apparently, there is a reasonable agreement between the two sets of data. Figure 6 shows the distribution of longitudinal residual stresses for three different currents at the position of  $z = 225$  mm. In all samples, the higher residual stresses were found in low carbon steel part. It may be attributed to the mechanical properties of the employed steels. In general, the material with higher yield stress can tolerate higher residual stresses particularly when the material experiences severe thermal gradients.

**Table 6** The predicted and experimental weld pool dimensions

Sample	Predicted (mm)	Experimental (mm)
105LP		
W1	4.33	4.6
W2	3.11	3.35
120LP		
W1	5.44	5.85
W2	4.6	4.1
135LP		
W1	6.16	7.39
W2	5.68	5.77

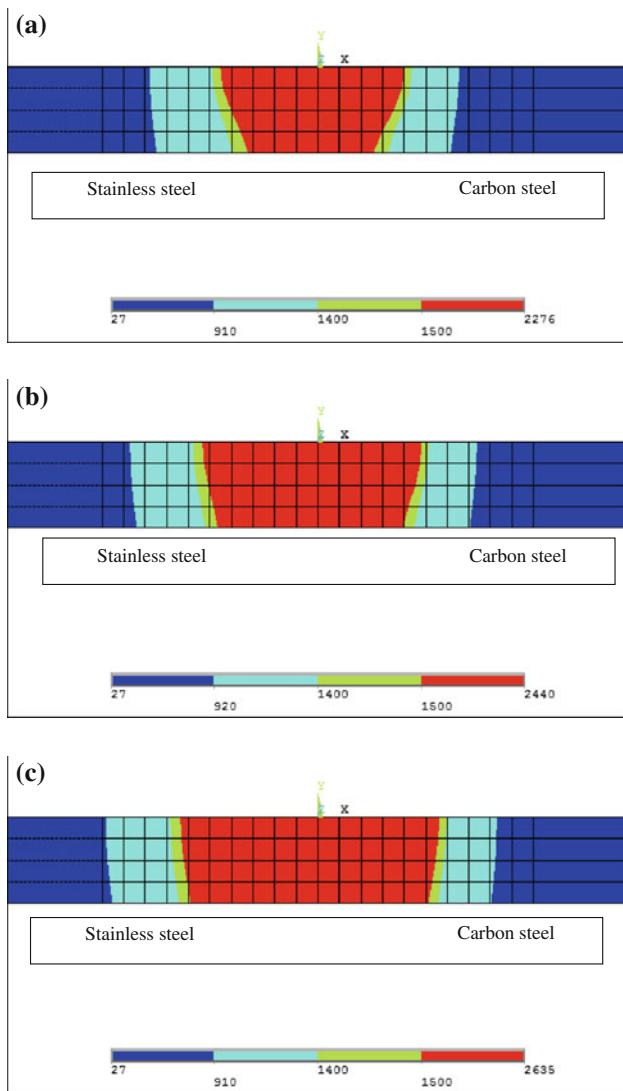


**Fig. 3** The effect of welding current on temperature distribution for long samples, **a** current of 105 A, **b** current of 120 A, **c** current of 135 A

Thus, higher yield stress of low carbon steel, i.e., 290 and 210 MPa for ferritic stainless steel, means that higher residual stresses can be produced in this part. It is worth

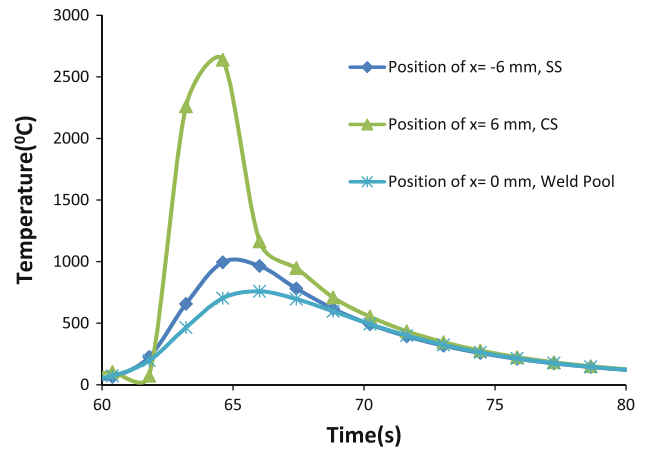


**Fig. 4** The temperature cycles at three different points for sample 120LP

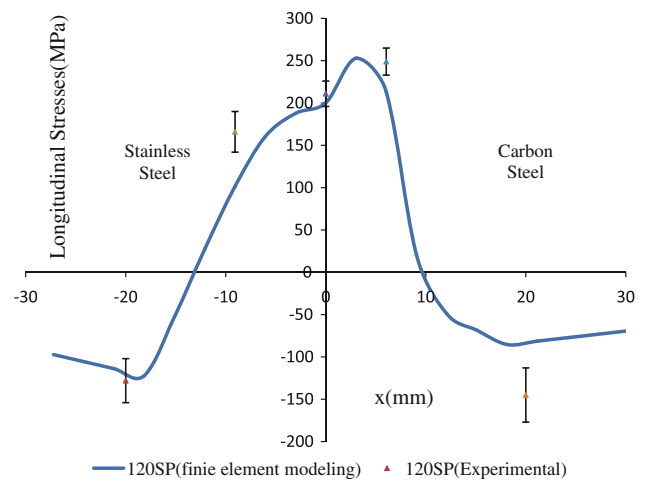


**Fig. 5** Comparison between the predicted and the experimental longitudinal residual stresses for sample 120SP

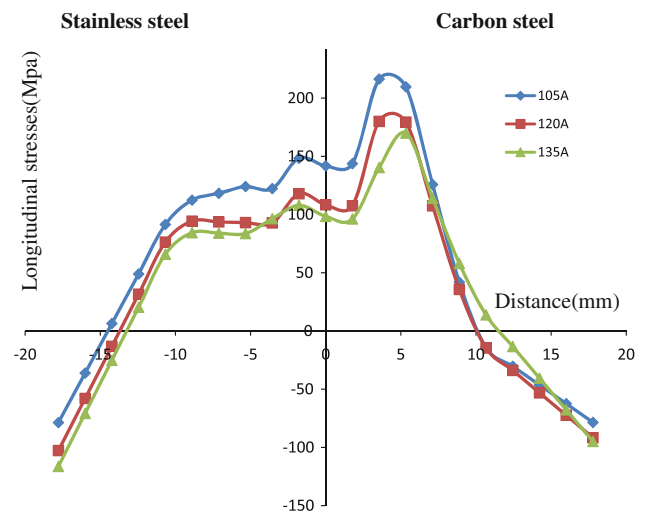


**Fig. 6** The effect of welding current on longitudinal residual stresses in the long samples under the forward welding sequence



noting that tensile stresses existing near the weld line are balanced with the compressive stresses. Figure 6 also shows that the peaks of tensile stresses in these samples decreased as the current increases. The possible reason is that higher welding current leads to plastic deformation and it contributes to relaxation of the thermo-mechanical stresses. In addition, Fig. 7 presents the distribution of transverse residual stresses. The results show almost a trend similar to that of longitudinal stresses.

Figures 8 and 9 indicate the effect of specimen length on longitudinal and transverse residual stresses in the middle of the welded parts. These figures show that longer sample undergoes lower residual stresses in the central region of the joint. In Fig. 10, the deformed shape of the welded plates is compared with  $y$ -displacement distribution. The maximum deflection of long sample, i.e., 120LP, was about five times of that for shorter one, i.e., 120SP. In other words, longer samples show lower stiffness due to the effect of their length and consequently, the resistance of this sample on deformation decreases. On the other hand, the higher deformation results in more relaxation of the induced stresses and thus it is expected that the lower amount of residual stresses are produced inside the long sample as shown in Figs. 8 and 9. The effect of welding sequence on longitudinal and transverse residual stresses was investigated for three different programs as mentioned in Table 5. Figure 11 shows the schematic illustration of the employed welding sequences. The distributions of longitudinal, transverse, and in the  $z$ - $x$  plane stresses are displayed in Figs. 12, 13, and 14, respectively. Obviously, the welding sequence changes the values and distributions of residual stresses. The results indicate that the symmetric welding sequence can be considered as an efficient welding

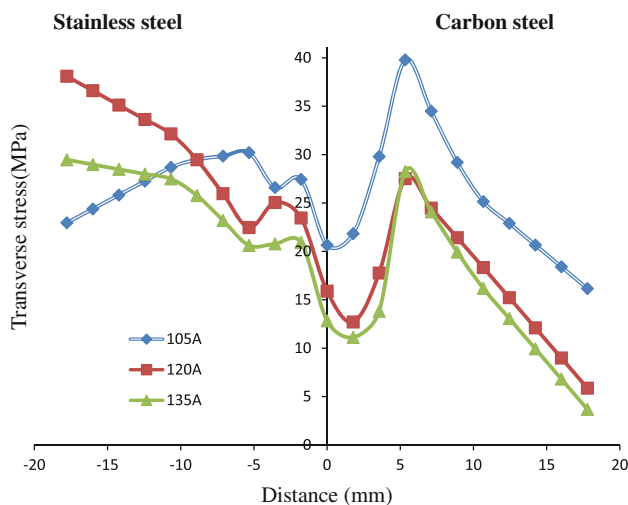


**Fig. 7** The effect of welding current on transverse residual stresses in the long samples under the forward welding sequence

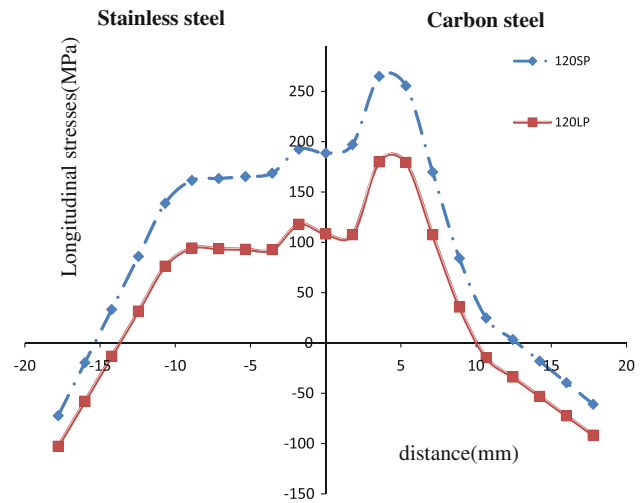


**Fig. 8** The effect of specimen length on longitudinal residual stresses for the forward welding layout

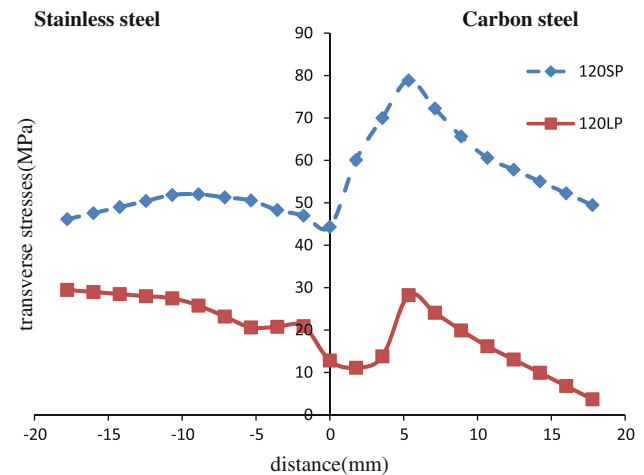


**Fig. 9** The effect of specimen length on transverse residual stresses for the forward welding layout

route in reducing residual tensile stresses. It may be due to lower thermal stresses coming from this layout while this effect is more pronounced for the material with the higher yield strength, i.e., low carbon steel.

## Conclusions

In this study, a three-dimensional finite element model was utilized to predict the effect of welding process parameters on the temperature and stress fields during and after dissimilar weld of CK4 and AISI409 using automatic TIG welding. Also, experimental measurements employing macro sectioning and X-ray diffraction were conducted to assess the weld pool shape and longitudinal residual stresses within the welded sample. The results show that:

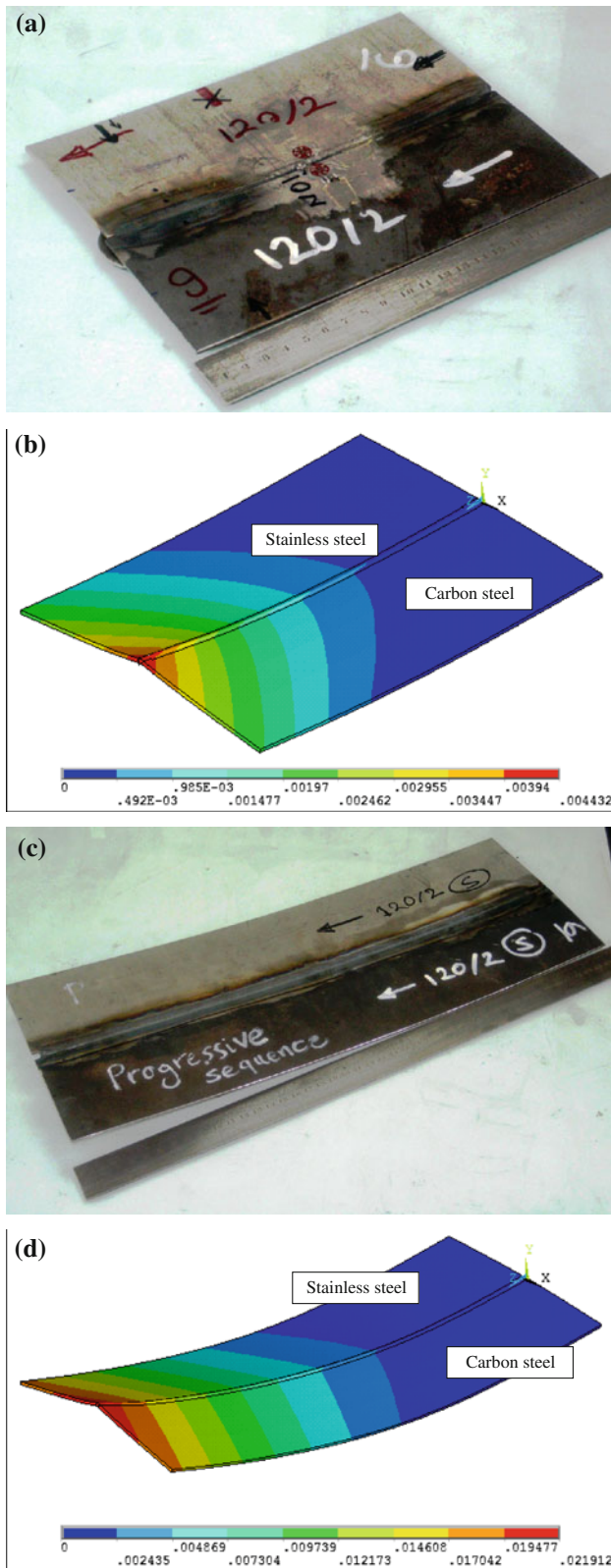


**Fig. 10** The effect of specimen length on welding distortion for the forward welding layout **a** sample 120SP, experimental; **b** sample 120SP, predicted; **c** sample 120LP, experimental; **d** sample 120LP, predicted

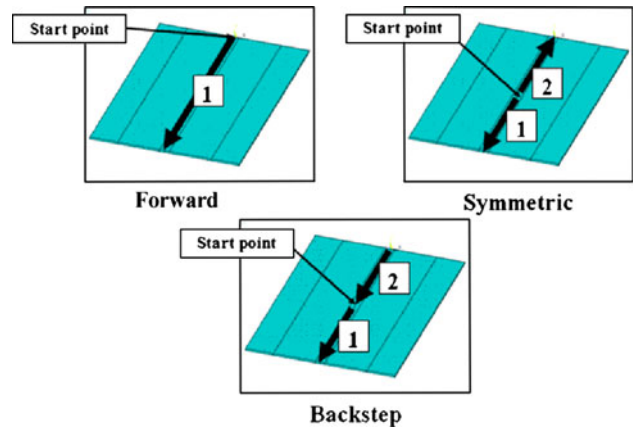


**Fig. 11** Schematic illustration of the employed weld sequences

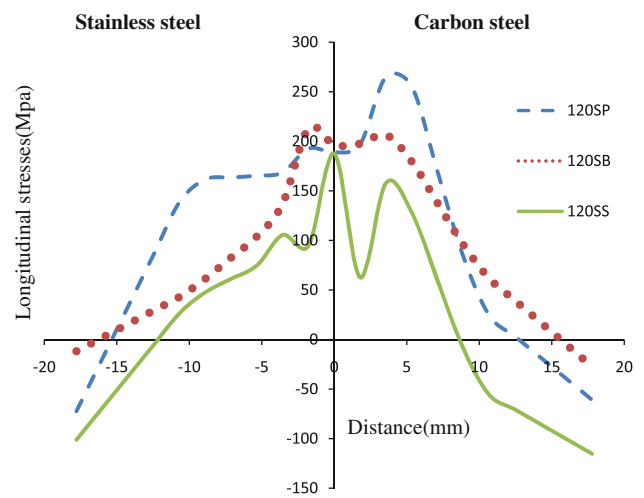


**Fig. 12** The effect of welding sequences on longitudinal residual stresses in the samples with the length of 225 mm

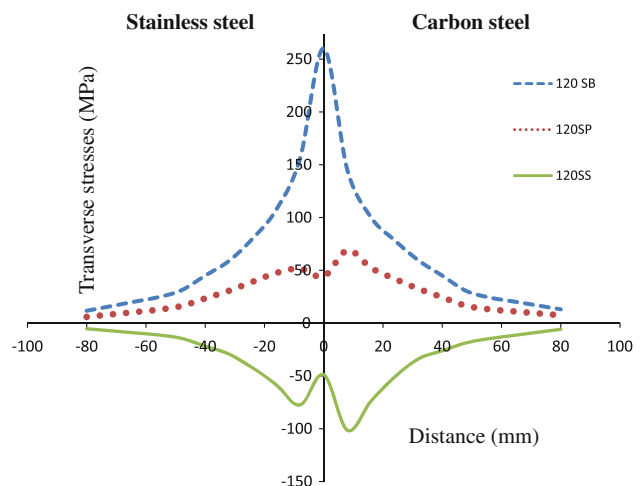


**Fig. 13** The effect of welding sequence on transverse residual stresses in the samples with the length of 225 mm

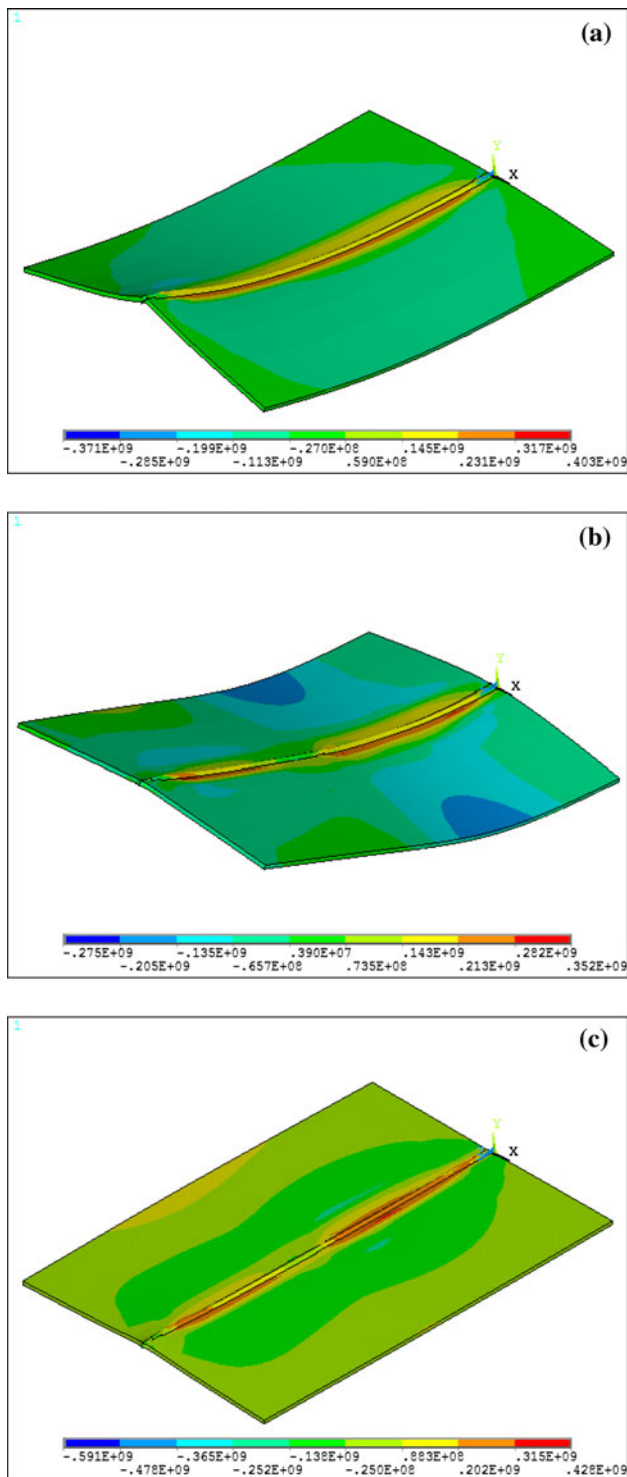


**Fig. 14** Distribution of residual stresses in  $z$ - $x$  plane in the samples with the length of 225 mm, **a** 120SP, **b** 120SB, **c** 120SS

1. There is a reasonable agreement between the predicted and the measured weld pool geometry and residual stresses that verifies the validity of the employed model.
2. In the dissimilar weld, the maximum residual stresses were found in the carbon steel part with the higher yield strength.
3. The maximum tensile residual stresses decreases with the increase in the sample length while the weld distortion increases.
4. Symmetric welding sequence shows to be an effective way to reduce the tensile residual stresses particularly in the middle of the joint compared to the other welding sequences employed in the this study.

## References

1. Kou S (2003) *Welding metallurgy*. Wiley, New Jersey
2. Choi J, Mazumder J (2002) *J Mater Sci* 37:2143. doi:10.1023/A:1015258322780
3. Paradowska AM, Price JWH, Ibrahim R, Finlayson TR (2006) *J Achiev Mater Manuf Eng* 17:385
4. Teng T, Lin C (1998) *Int J Press Vessel Pip* 75:857
5. Teng T, Chang T, Tseng W (2003) *Comput Struct* 81:273
6. Katsareas DE, Yostous AG (2005) *Mater Sci Forum* 490–491:53
7. Sahin S, Toparli M, Ozdemir I, Sasaki S (2003) *J Mater Process Technol* 132:235
8. Akbari D, Sattari-Far I (2009) *Int J Press Vessel Pip* 186:769–776
9. Saedi HR (1983) *Transient response of plasma arc and weld pool geometry for GTAW process*. PhD Thesis, Massachusetts Institute of Technology
10. Belytschko T, Liu WK, Moran B (2000) *Nonlinear finite element methods for continua and structures*. Wiley, Chichester, England
11. Abid M, Siddique M (2005) *Int J Press Vessel Pip* 182:860
12. Taljat B, Radhakrishnan B, Zacharia B (1998) *Mater Sci Eng A* 246:45
13. De A, DebRoy T (2004) *J Appl Phys* 195:5230